Influence of Visible Wavelengths in Laser-Based Soldering Applications

Jan Brüggenjürgen[*1,2], André Häusler[1], Alexander Olowinsky[1], and Arnold Gillner[2]

[1]*Fraunhofer Institute for Laser Technology ILT, Aachen, Germany*
[2] *Chair for Laser Technology LLT, RWTH Aachen University, Aachen, Germany*
[*]*Corresponding author's e-mail: jan.brueggenjuergen@ilt.fraunhofer.de*

Recent innovations in UV and visible laser sources have led to more efficient and precise processes for electronic applications. This study presents a detailed comparison of blue (450 nm) and green (515 nm) laser wavelengths against established infrared (975.3 nm) sources. Through qualitative comparisons, we analyse energy coupling and absorptivity in solder and terminal materials, identifying significant performance differences across the wavelength spectrum. A double integrating sphere setup is used to capture in-situ diffuse and laser back reflections, enabling a thorough evaluation of energy deposition during soldering. Correlating data from detectors in both spheres provides a more holistic understanding of energy behaviour, supporting improved emission-based control techniques such as pyrometry. Our results demonstrate that shorter wavelengths—particularly blue and green—offer enhanced energy absorption, leading to more efficient soldering with reduced damage on surrounding components. Across the tested alloys, visible wavelengths increased static absorptivity versus 975 nm by up to ~50%, and green (515 nm) reduced the activation energy for OK joints by ~24% relative to blue (450 nm) and ~50% relative to IR. Shear testing on header–via samples showed comparable peak forces for blue and green (~200 N) and lower values for IR (~180 N). The findings not only advance laser soldering technology but also support its broader industrial adoption, aiding the transition toward greater electrification and sustainability in manufacturing.

DOI: 10.2961/jlmn.2026.02.2006
Keywords: laser soldering, visible wavelengths, integrating sphere, energy efficient, reflected-radiation damage reduction, energy absorption, electronic assemblies

1. Introduction

Laser-based soldering has become an established joining technique in niche applications where batch soldering methods lack accuracy, such as in repair [1-3] or recycling processes [4,5]. Progressive miniaturisation and increasing demands for sustainability favour highly flexible, precise, and localised soldering methods [1,6,7]. However, major drawbacks of laser soldering are its setup and operation costs. Fibre lasers typically reach efficiencies of only about 50% [8]. Furthermore, converting this laser radiation into heat at the junction site can result in additional energy losses of up to 70% [9] due to reflection.

Recent advancements in laser technology offer promising solutions. By switching to newer diode lasers, which can achieve efficiencies of up to 73% [10] and provide wavelengths more suitable for soldering—specifically, moving away from infrared and into the visible range—substantial efficiency gains are still obtainable [11]. This shift not only reduces operational costs through energy savings but also improves process reliability by lowering immediate risk of surrounding component damages and environmental sustainability by increasing yield and lowering carbon footprints. Thus, these developments make laser-based soldering increasingly viable for a broader range of industrial applications.

2. Objectives

An informed decision for a laser soldering wavelength requires absorption measurements at room temperature and in-situ measurements for different wavelength-solder combinations. This study offers calibrated, validated and physically tested in-situ absorption and coupling coefficient measurements for 450 nm (blue), 515 nm (green) and 975 nm (IR) to compare their interactions with solder's energy absorption, flux activation and forming a sound joint.

3. Material and Methods

Measuring in-situ absorption and coupling coefficients during laser soldering can be challenging due to elevated operating temperatures, limited equipment space and danger of equipment damage. An experimental setup based on Ulbricht or integrating spheres can capture reflected radiation.

3.1 Double integrating sphere

As a single sphere cannot capture back reflections, a second sphere is used in combination with a 90:10 beamsplitter (see Figure 1). Such a setup was already successfully tested in previous works [12]. The beam path starts after the respective focus optics and enters the beamsplitter, 10 % are directly reflected and lost for the experiment, therefore captured in a beam trap. The remaining 90% continue out of the beamsplitter and into the lower Ulbricht sphere from the top. The sample of interest is placed into the beam path inside the lower sphere and reflects diffusely as well as directly back into the beam path. Diffuse reflections are guided through multiple reflections to the observation port on the right. Inside a reflective bandpass filter selects the wavelength of the utilized laser and avoids recording of process emissions. A photodiode (DET10A2 / DET10N2 Thorlabs) quantifies the incident light into voltage measured through a DAC setup.

Direct back reflections travel up outside the lower sphere and get reflected on the beamsplitter again and into the upper sphere. Subsequent diffuse reflections guide the collected radiation into the observation port fitted with an identical reflective bandpass filter and photodiode. Potential higher order reflections through the beamsplitter are neglected as seen in the following calibration chapter.

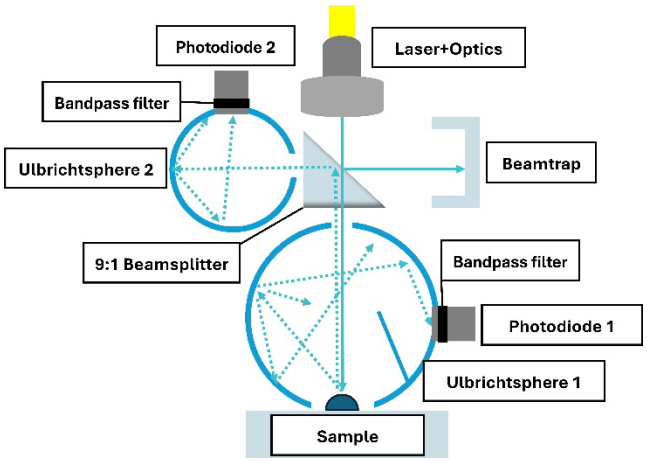

Figure 1 Experimental setup schematic with beam path for absorption measurements using two Ulbricht spheres for diffuse reflection (sphere 1) and back reflection (sphere 2).

Calibration of photo detectors

To account for leakage, wavelength dependent sensor response and setup variations, calibration is performed relative to the desired energy level for an artificial total diffuse and total back reflection. A broadband mirror (Thorlabs BB1-E02) is placed at the sample spot. The angle relative to the beamsplitter determines the reflection type as seen in Figure 2. If the mirror is placed at an angle (see Figure 2, (a)), the initial laser beam path is diverted onto the diffuse reflective barium sulfate surface of the first Ulbricht sphere. The detected voltage in the lower photodiode is recorded over multiple laser powers P_L (0%-100%). By computing the linear fit between detected voltage and expected power, the first reflected energy constant A_1 is computed. As the beam path into the lower sphere stays open between beamsplitter and sphere, minute amounts of diffuse reflection can escape back into the setup, get reflected at the beamsplitter and enter the second sphere. This results in a proportional response on the second photo detector that needs to be considered. By including a second correction factor as the linear fit between both detector responses, A_2 is calculated.

For back reflection, the mirror is placed flat into the lower sphere (see Figure 2, (b)). The initial beam path is diverted back into the beamsplitter and reflected into the second sphere. As before linear fits for detector power response (A_3) and their corresponding correction due to stray detection in the lower detector (A_4) are computed.

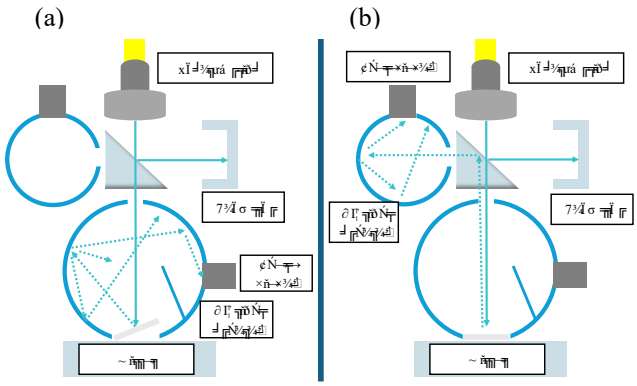

Figure 2 Schematic process of photodetector calibration for total diffuse reflection (a) and total back reflection (b).

Due to the nature of linear fits on idealized reflections, higher order reflections through the beamsplitter can be neglected. By combining both reflection measurements, formula 1 can be derived to quantify diffuse and back reflection.

$$\mathbf{P_R(U_1, U_2) = A_3 * \left(U_1 - (A_2 * U_2)\right) + A_1 * \left(U_2 - (A_4 * U_1)\right)}. \quad (1)$$

Equation 1 requires both photodetectors to have their respective zero intersection at 0 V when reaching 0 W laser power. Due to different wavelength response, utilized bandpass and ND-filter, zero crossings vary between utilized laser wavelengths by multiple Watts. To account for these, inter setup deviations, a correction term K_1 is introduced as the average of the difference between calculated laser power (using equation 1) and set power. Effectively recentring all photo detector responses to 0 W and 0 V and forming equation 2.

$$\mathbf{P_{R2}(U_1, U_2) = P_R(U_1, U_2) + K_1}. \quad (2)$$

Verification of calculated reflectance

To compare each calibrated detector setup against known ground truth data, four samples of known absorption coefficients were tested. Three of those (Cu-ETP, 14301-Steel and AW-6082) consist of raw rectangular cuts (as seen in Figure 3) placed directly under the lowers sphere aperture, while a hand painted cutout of copper painted 10 times with $BaSO_4$ is used to simulate a closed lower sphere.

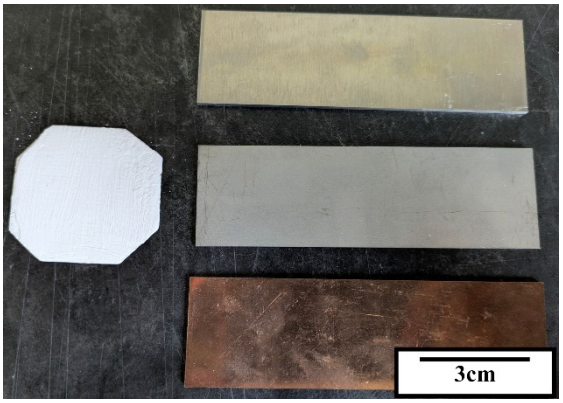

Figure 3 Validation reference samples used. $BaSO_4$ (left), AW-6082 (top right), 14301-Steel (middle right) and Cu-ETP (bottom right).

All samples were measured multiple times with a calibrated UV-Vis-NIR spectrophotometer Lambda 950 by Perkin Elmer. Their respective reflectance values can be seen in Table 1.

Table 1 Average spectrophotometer (n=3) reflectivity measurements of validation samples.

Laser	$BaSO_4$	Cu-ETP	AW-6082	14301-Steel
450 nm	96.0±1.8	32.5±0.2	38.5±1.1	53.1±0.3
515 nm	96.2±1.1	15.1±3.7	30.2±0.3	49.2±0.0
975 nm	97.1±0.4	89.2±0.5	63.3±2.2	61.6±0.1

Transmission values were assumed to be zero due to sufficient material thickness (greater than 2 mm). Following energy conservation and $P = P_A + P_R + P_T$, absorbed energy could be easily computed from reflected energy by $P_A = 100 - P_R$. By computing the difference of ground truth data (Table 2) and calculated reflectance values through the double spheres (Equation 2), the experimental setup can be validated.

Table 2 Absolute reflectance differences between measurements from Lambda 950 (Table 1) and calculated reflectance values from measurements (n=4) with double sphere setup and equation 2 (Error computed through error propagation as independent variables).

Laser	$BaSO_4$	Cu-ETP	AW-6082	14301-Steel
450 nm	22.0±1.8	9.6±2.0	1.8±1.3	0.5±0.7
515 nm	2.3±4.2	8.0±4.5	1.2±2.7	6.2±3.2
975 nm	4.0±1.3	4.3±0.9	8.2±2.5	8.3±0.9

3.2 Laser and optics

Three laser systems were used to facilitate comparison between wavelengths (Table 3). All sources utilize individual welding optics defocussed to d = 5.3 mm for the absorbance tests (the aperture of the sample holder) and d = 5.9 for coupling coefficients, while yielding a gaussian beam profile.

Table 3 Utilized laser and their measured optical characteristics.

Laser	λ[nm]	P_{Peak}[W]	$w_0[\mu m]$	M^2	$Z_R[mm]$
Nuburu AO-150	450	150	351.11	118.0	7.29
Dilas compact evolution	976	150	482.1	32.17	23.28
Trudisk 1020	515	1000	68.7	23.3	1.194

3.3 Solder wires and material samples

Given a near infinite mix of flux compositions, one flux family (GUMMIX) was selected with a variety of elemental solder sub compositions. Commonly available mixes of Sn3Ag0.5Cu were tested as well as rarer Sn0.3Ag0.7Cu2Bi0.035Fe (as seen in Table 4). Their flux percentage varied between 2.5% and 3.5%. CuSn6 chips were used as binding sites in absorbance measurements (see Figure 4, (a)) and FR4 substrate, 70 µm tin-plated printed circuit board (PCB) (see Figure 4, (b)) in activation energy and coupling coefficient measurements.

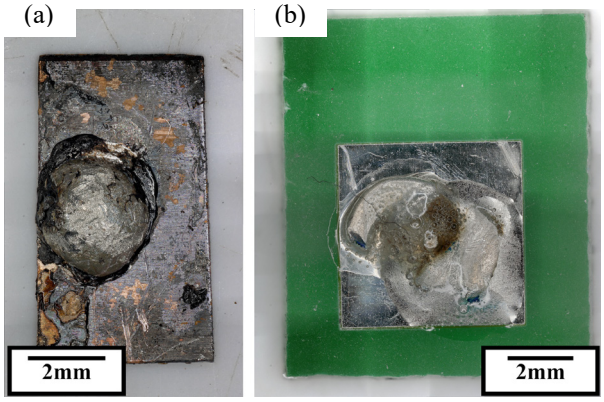

Figure 4 Used carrier samples after absorbance test ((a), on CuSn6) and activation energy ((b), PCB).

The respective reflectance at room temperature was measured by accumulating a coil of wire (>10g) and compressing it through a four-ton hydraulic press into a flat sheet. All were tested inside the spectrophotometer for reference (see Figure 5). Absorbance spreads widely (up to 30%) between solder alloys but stays consistent between flux percentage variations. The desired increase in absorptivity by up to 50 % from IR to visible wavelengths can be observed as well (SB RMA LFM 48 2.5%). HF LFM-48 3.5% marks an outlier by favouring 515 nm over 450 nm in terms of

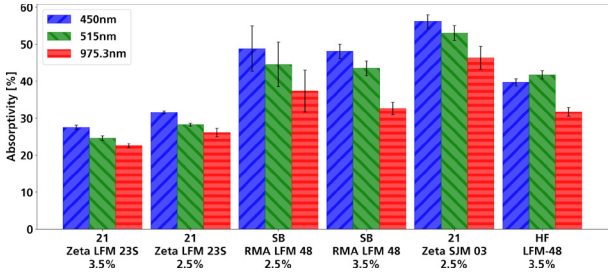

Figure 5 Absorptivity of tested solder wires at room temperature (21°C) for relevant laser wavelengths (450 nm, 515 nm and 975 nm) (N = 3).

Table 4 Utilized solder wire samples.

Name	Melting point [°C]	Flux [%]	Sn [%]	Ag [%]	Cu [%]	Bi [%]	Ni [%]	Fe [%]
SB RMA LFM48	217-220	2.5	96.5	3	0.5			
SB RMA LFM48	217-220	3.5	96.5	3	0.5			
HF LFM-48	217-220	3.5	96.5	3	0.5			
21Zeta SJM-03-S	210-226	3.5	96.965	0.3	0.7	2		0.035
21Zeta LFM 23S	228-229	2.5	99.315		0.6		0.05	0.035
21Zeta LFM 23S	228-229	3.5	99.315		0.6		0.05	0.035

absorptivity, which could be attributed to flux composition adjustments made by the manufacturer for HF classification.

4. Results and Discussion

Characterizing the absorption coefficients during the laser soldering process can be ambiguous due to process emissions, a plume forming from evaporating flux and overall geometric instability of the solder during liquidation and solidification phases.

4.1 Absorption coefficients

Rather than characterizing in-situ, the required melting energy will first be introduced through an external heater from below the sample. Laser power (P_L) is reduced to minimal possible amount in terms of stable emission power and ratio of rise to hold time. All setups were calibrated using a PM100D power meter from Thorlabs as power in the system P_S. By heating all solder samples past their liquidus temperature, they form hemisphere due to surface tension, providing an ideally flat test surface. The lower Ulbricht sphere is also flooded with nitrogen as an inert gas to remove flux vapours and prevent oxidization.

The probe parameters were chosen such that the additional temperature rise during each pulse remained modest compared to the externally imposed base temperature. Even for 450 nm the estimated transient increase is ≈ 40 K, and only ≈ 12 K and ≈ 5 K for 515 nm and 975 nm, respectively (see Table 5). Given that the base temperatures span 150–300 °C and each temperature level is probed only once, the measurements are dominated by the quasi-static temperature defined by the external heater rather than by the probe-induced heating.

Samples are mounted on an aluminium cylinder into the lower Ulbricht sphere. Due to the limited space a wire feeder robot is impractical. Rather, 20 mm of d = 0.8 mm wire is wound to a spiral and pressed to form a flat cylinder. The sacrificial CuSn6 chip is slid in place first and the solder wire cylinder press fits into form (see Figure 6); the surface tension forms the desired ball shape.

Table 5 Used laser parameters and estimated temperature increase for each sample.

Laser	P [W]	t [ms]	Ep [J]	Estimated ΔT per sample [K]*
450 nm	49.9	20	1.00	41,88
515 nm	45.9	10	0.46	12,38
975 nm	11.0	20	0.22	4,62

Calculated for the solder volume corresponding to 20 mm of 0.8 mm wire ($m \approx 7.3 \times 10^{-5}$ kg, $\rho = 7310$ kg/m³, $c = 227$ J/(kg·K)), using typical high-temperature absorptivity (70% / 45% / 35% for 450 nm, 975 nm)

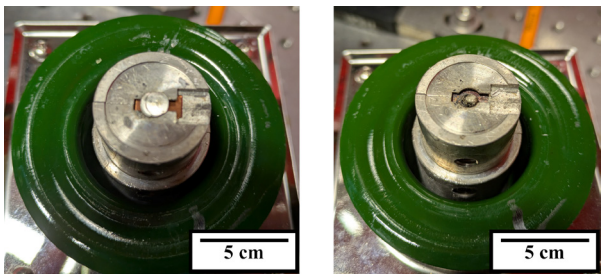

Figure 6 Loading of a solder material sample (a) and after a heating cycle (b).

A PT1000 element measured the core temperature of the cylinder during the process and triggered 7 laser pulses at: 250°C, 275°C, 300°C, 225°C, 200°C, 175°C and 150°C. The heating from 150 °C to 300 °C took approximately 15 minutes, and the subsequent cooling phase from 300 °C back to 150 °C lasted approximately 10 minutes. The heater was turned off automatically when reaching 300°C. Temperature deviations between the sample holders' surface and core were accounted for by a linear fit model calculated from room temperature and solders melting point verified through an observation port on the Ulbricht sphere.

$$P_{R3}(U_1, U_2) = P_{R2}(U_1, U_2) * K_2 \,. \quad (3)$$

Table 6 Computed coefficients for reflected power calculations used in equation 3.

Laser	$A_1[\frac{W}{V}]$	A_2[-]	$A_3[\frac{W}{V}]$	A_4[-]	K_1[W]	K_2[-]
450 nm	41.23	0.41	51.42	0.07	-5.90	1.06
515 nm	45.86	0.05	48.39	0.01	-1.42	0.98
975 nm	5.16	0.05	3.95	0.01	-0.06	1.30

The sample holder introduces a protruding structure into the lower sphere which also does have a lower reflectivity than the spheres surface. To account for any reflection losses, a second calibration coefficient K_2 is introduced to equation 2 and forms equation 3.

Placing the holder into the setup holding only a CuSn6 chip but no solder material and measuring the absorptivity, K_2 can be calculated by comparing it against previously obtained ground truth data from the spectrophotometer. Table 6 shows all used calibration and correction coefficients. The difference in detector responsiveness of the biased detectors (DET10A2 for 450/515 nm and DET10N2 for 975 nm) can be directly observed by the calculated A_1 and A_3 values needing up to ten times more intensity per registered one volt. Factor K_2 for 515 nm falling below one, suggests a slight misalignment during the calibration step as the sample carrier will not provide additional radiance but rather an attenuation surface.

Figure 7 shows the result for the 450 nm experiment series. A slow linear rising pattern in absorptivity can be observed during the heating phase (250 - 300°C), followed by jumping up to 10% when testing at solidification again (225°C). The final absorptivity remains roughly constant during the cooling phase (225-150°C). HF LFM 48 3.5% outperforms all other solders by up to 10% with a stronger linear gradient during the heating phase. A possible explanation for the overall trend is the boiling flux initially diffusely scattering incoming laser radiation as well as deforming the solder surface which solidifies again, deviating from a quasi-circular surface assumption. Comparing against 975 nm results in Figure 8, yields a similar picture at a lower absolute absorptivity.

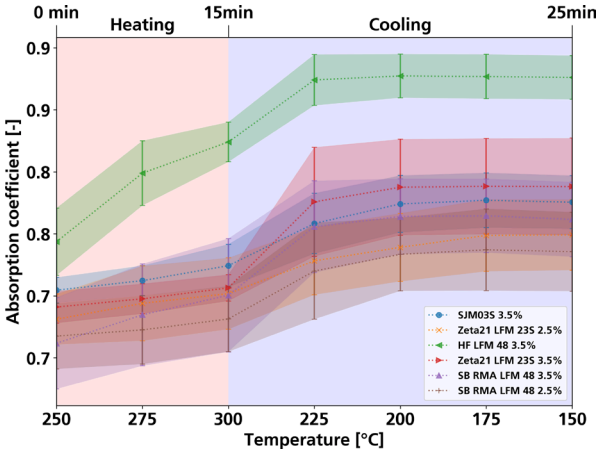

Figure 7 Absorption measurements of different solder types for 450 nm, chronologically sorted temperature axis (marked heating (15 min) and cooling cycle (10 min)) (N = 3).

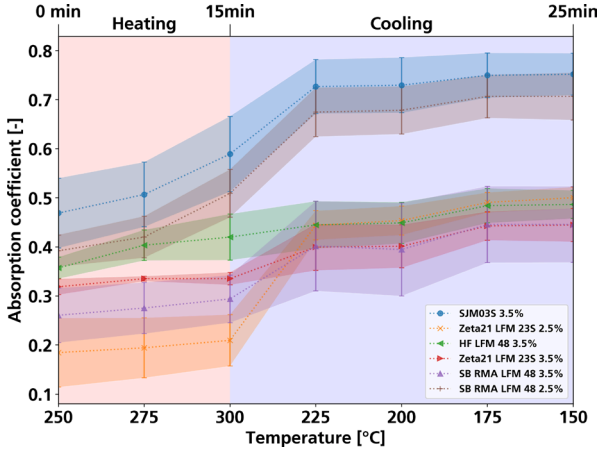

Figure 8 Absorption measurements of different solder types for 975 nm, chronologically sorted temperature axis (marked heating (15 min) and cooling cycle (10 min)) (N = 3).

Aggregating all performed experiments by averaging individual solder samples for each laser wavelength shows the expected gradation (see Figure 9). Blue wavelengths outperform both green and infrared. While all three series experience a step effect during the release of flux, 450 nm displays the lowest difference of only 0.1, while 515 nm and 975 nm step at least twice as much. A possible explanation could be reduced interactions of blue wavelengths with the selected GUMMIX flux family or increased early coupling due to minor increased intensity of the sampling beam.

Observed increases in absorption at shorter wavelengths are consistent with Drude-type behaviour of metals, where the real part of the refractive index and resulting reflectance decrease from IR toward the visible for Cu, Sn and Ag constituents of the solder and terminals [13]. Quantitatively, the measured increase in absorptivity from 975 nm to the visible range (up to ~50 % for SB RMA LFM 48 2.5 %, Figure 5) is comparable to the improvement reported by Tatsumi et al. [11] for blue-laser soldering of Sn-Ag-Cu, who observed a ~43 % increase relative to IR. This agreement supports the interpretation that the dominant trend is governed by the optical properties of the solder and terminal materials.

To assess the influence of irradiance and heating rate on the apparent absorptivity, additional control measurements

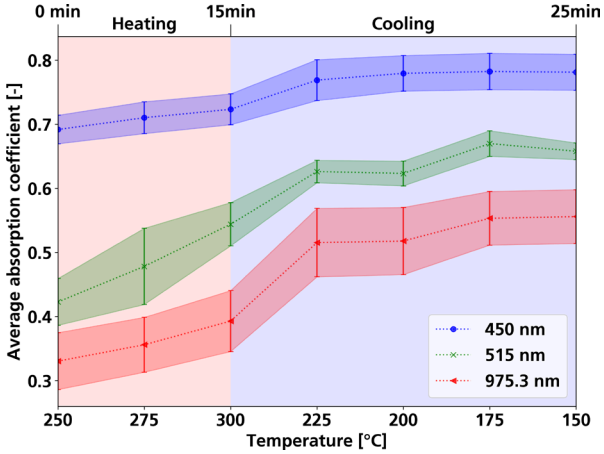

Figure 9 Averaged absorption measurements of different solder for 450 nm, 515 nm and 975 nm, chronologically sorted temperature axis (marked heating (15 min) and cooling cycle (10 min)) (N = 3).

were performed at 975 nm with laser powers of 15, 19 and 24 W (identical spot size and pulse duration). The measured absorptivity changed by at most ~1 percentage point across these settings, i.e. within the repeatability of the setup, indicating only a weak dependence on irradiance in the investigated range.

4.2 Coupling coefficients

By removing the heated sample holder, a switch to active monitoring of coupling coefficients is performed. The energy needed for flux activation and phase change of the solder wire is delivered by the laser assemblies. Recording both photodetectors continuously during the soldering process provides insights into changing coupling coefficients over time. In Figure 10, an example of such a process can be seen. Unexpectedly, the overall coupling coefficient drops during the soldering process from 0.61 to nearly 0.37 marking a reduction by up to 50%. Similar trends can be observed for all wavelengths tested. By plotting back reflection and diffusion photodetector response as well, it can be observed that the increase in diffuse reflections contributes most to lowering the coupling. A possible explanation could be the

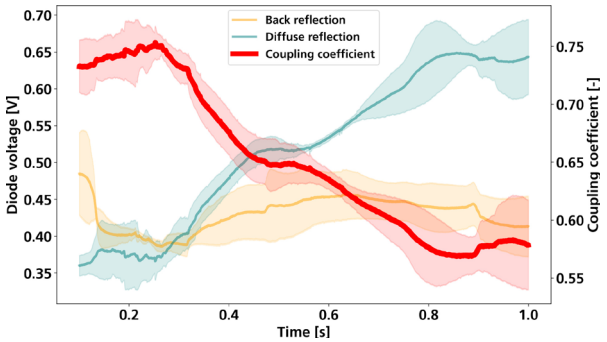

Figure 10 In-situ coupling coefficient, averaged over three experiments (t = 1 s, Ps = 60 W, λ = 450 nm).

boiling of flux, forming a diffusive layer at the top of the solder pool. A gaseous plume formed by vaporized flux could also interfere with the designated beam path. The observed drop in coupling coefficient and concurrent rise in diffuse reflection (Figure 10) are consistent with previous measurements of dynamic reflectivity in laser soldering and

welding [9,14], where evolving melt-pool geometry and process plumes were shown to significantly modify the effective absorptance during the interaction time.

4.3 Activation energy

Performing visual inspection on soldered samples from coupling coefficient test allows for classification into OK and NOK samples. Varying process parameters such as holding time t and laser power P_S can generate a process map for every solder wire and laser pair. Plotting these results into a process map, should produce a plateau of OK samples surrounded by NOK samples. Low energy input results in a lack of bonding, too high energy destroys the substrate or even vaporizes parts of the solder. Approaching the axis borders also leads to NOK. Reducing process time while increasing laser power is limited due to heat capacity and heat transfer. Following the laser power down while increasing process time will fail due to parasitic heat flows out of the junction site, never yielding high enough energy concentration for solder to melt. Examples of the lower left boundary can be seen in Figure 11. Comparing all process maps between solders and laser sources displays a counterintuitive trend of 515 nm wavelengths requiring less energy to form sufficiently strong OK bonds compared to 450 nm (see Table 7).

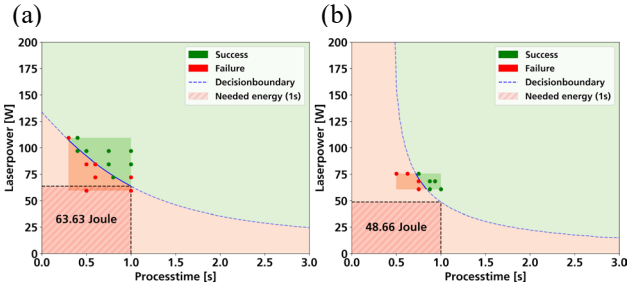

Figure 11 Process maps for SJM03S solder with decision boundary fit and t = 1s energy interpolation ((a) 450nm, (b) 515nm).

4.4 Shear strength

To evaluate the quality of the soldered joint, tests using a header-via connection were performed. A specially designed carrier allowed multiple soldering tests in series (see Figure 12). A grid search was performed by altering laser power and process time until either lacking wick effect or burning/delamination of the pcb was observed.

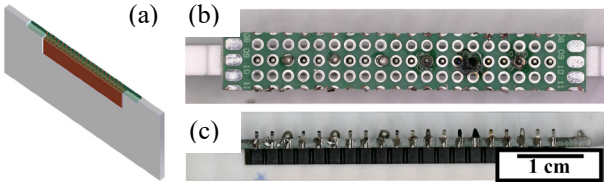

Figure 12 Example carrier used for header-via connection tests. Schematic (a), top view (b) and side view (c).

After soldering, the individual joints are extracted by cutting between the empty pin sets with a band saw. A shear tester individually tests up to 200 N by pushing against the connection from the backside (black spacer side) and recording the experienced back push. Determining the maximum and standard deviation from the largest three samples for each series and wavelength allows for comparisons between setups (see Figure 13).

Table 7 Fitted activation energies per solder and laser (lowest per laser marked grey, average in last row).

Name	450 nm	515 nm	975 nm
SB RMA LFM48 2.5%	85.15 J	63.91 J	131.38 J
SB RMA LFM48 3.5%	88.99 J	53.23 J	109.79 J
HF LFM-48 3.5%	73.26 J	58.36 J	104.74 J
21Zeta SJM-03-S 3.5%	63.63 J	48.66 J	126.57 J
21Zeta LFM 23S 2.5%	87.91 J	73.98 J	164.01 J
21Zeta LFM 23S 3.5%	86.34 J	69.76 J	139.78 J
ø	**80.88 J**	**61.32 J**	**129.38 J**

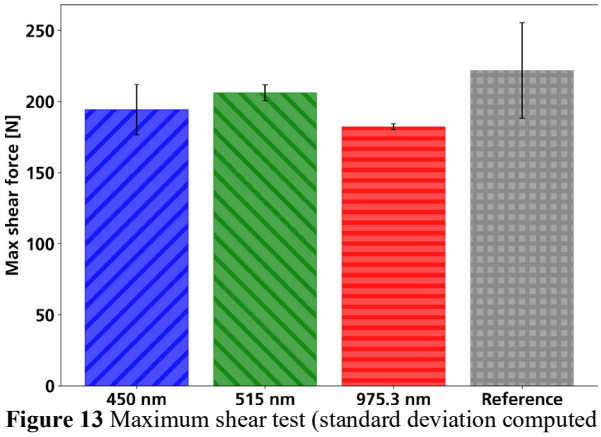

Figure 13 Maximum shear test (standard deviation computed from top 3 samples) results for every laser source. Reference data from hot air soldering (t = 60s, T = 400°C).

A reference is obtained by hand soldering a carrier of samples with a heat gun at 400°C and a holding time of t = 60 s. 450 nm and 515 nm seem to produce equally strong connections resisting destruction with a peak shear force (consistent with literature findings [11]) of around 200 N. The 975 nm results placed last (180 N) while providing the most consistent measurements. All laser soldered samples fall short of the hand soldered specimens, which could be the result from more uniform heating. Still all samples provide sufficiently large shear resistance and visible wavelength even outperformed IR at lower energy requirements. The fact that all laser-soldered joints reached shear strengths close to the hand-soldered reference is in line with previous comparisons between laser and conventional reflow soldering, where laser processes produced mechanically competitive joints when process parameters were optimised [15]. Our results extend these findings to visible wavelengths and header–via geometries.

4.5 Influence of laser parameters and limitations

A limitation of this study is that the three laser sources could not be operated with fully identical parameter sets. In the absorption experiments, the available power and minimal pulse duration led to different pulse energies and irradiances for each wavelength (Table 5), and hence to different transient temperature rises of the molten solder. Based on the solder volume and thermal properties, the probe-induced temperature increase per pulse is estimated as ≈ 42 K for 450 nm, ≈ 12 K for 515 nm and ≈ 5 K for 975 nm. These differences in ΔT can in principle influence temperature-dependent absorptivity, flux behaviour and wetting, and must therefore be considered when interpreting the results.

At the same time, the magnitude of these effects appears to be small compared to the wavelength trends. Across all alloys, the static and in situ measurements show increases in absorptivity of up to ~50 % when going from 975 nm to the visible (Figure 5 and Figure 9). In contrast, additional control measurements at 975 nm, where the laser power at the sample varied between 15, 19 and 24 W at constant spot size and pulse duration, changed the measured absorptivity by only about 1 percentage point. Within the parameter ranges studied here, the apparent absorption therefore depends much more strongly on wavelength than on the moderate variations in irradiance and probe-induced heating. Nevertheless, the reported absorption levels, coupling coefficients and activation energies should be understood as effective process quantities that convolve wavelength, irradiance and thermal history rather than isolating a purely intrinsic wavelength effect.

5. Conclusion

In this paper, a thorough investigation into the absorption behaviour during laser soldering with visible and IR wavelengths was performed. A two Ulbricht sphere setup for reflectivity measurements was designed. Static and in-situ tests revealed a rising absorptivity after loss of flux through long heating cycles while a falling absorption is observed during in-situ monitoring.

450 nm has proven as a desirable wavelength choice within the tested process windows due to higher coupling coefficients and comparable junction strength. It provides up to 50 % increase in initial absorption (compared to 975 nm) and maintains this lead during the full soldering process. Although the probe and process parameters (pulse energies, durations and irradiances) could not be fully matched between the three sources, they were selected to keep the additional probe-induced heating relatively low, and control tests at 975 nm showed only ~1 % variation in absorptivity when changing power. The observed advantages of visible wavelengths therefore appear to be dominated by wavelength effects, even though secondary influences of the non-uniform parameters cannot be completely excluded. These results align with previous results from Tatsumi et al. who observed a 43% improvement [11].

515 nm did show promising low overall activation energy requirements for soldering, possibly resulting from higher interactions with the utilized flux family. These lower apparent activation energies are obtained under different power–time combinations for each source and should thus be interpreted as process-level trends rather than a purely intrinsic material property.

As shown, visible wavelengths offer key advantages for soldering and may serve as a future manufacturing method with lower energy consumption in a variety of applications.

Acknowledgments

(1) This project has received funding from the IGF (No 22.770N) through the DVS (No 10.3608) titled “Grundlagenuntersuchung zum Laserstrahllöten im sichtbaren Wellenlängenbereich für bauteilangepasste Energieeinbringung “

(2) The data that support the findings in this study are available upon reasonable request. Selected data are available after authorization in Coscine with the persistent identifier (PID) http://hdl.handle.net/21.11102/ba8f12ce-d404-4d41-bb44-8ac00c8636b1 (accessed on June 30, 2025). For further information, please contact the corresponding author.

References

[1] J. Wang, Z. Wu, and J. Qiao: “Research on Laser Repair Technology for Micro-LED Display Chips,” Proc. 2024 IEEE Int. Conf. Manipulation, Manufacturing and Measurement on the Nanoscale (3M-NANO), (2024) 307.

[2] E. G. Bakhoum and K. M. Van Landingham: “Precision Repair of Defective Soldering Joints with Gold Nanoparticles and a Low-Power Laser: Tackling a very old problem with new technology,” IEEE Nanotechnol. Mag., 10, (2016) 25.

[3] A. A. Ismail, M. A. Bakar, A. Jalar, Z. E. Zolkefli, E. Basiron, and M. N. Ilias: “Laser Rework Process for Efficient Lead-Free Solder Joints Ball Grid Array (BGA) Component Rework,” IEEE Trans. Compon., Packag. Manuf. Technol., 14, (2024) 735.

[4] B. Choi, B. Dominguez, A. D'Souza, H. Khadse, A. Kunkel, S. Nagarajan, T. Necke, R. Peche, M. Revello, and J. Rossa: “Sustainable recycling process for tantalum recovery from printed circuit boards,” Resour. Conserv. Recycl., 198, (2023) 107201.

[5] G. Kuznetsov, M. Kats, and I. Kats: “Laser Technology for Use in Recycling Printed Circuit Boards,” Chem. Pet. Eng., 58, (2022) 491.

[6] L. Stauffer, F. Walti, U. Vokinger, and K. Siercks: “High-precision surface mount assembly of micro-optical components per laser reflow soldering: Positioning accuracy and thermal stability,” Proc. SPIE, 5454, Micro-Optics: Fabrication, Packaging, and Integration, (2004).

[7] A. Gillner, J. Holtkamp, C. Hartmann, A. Olowinsky, J. Gedicke, K. Klages, L. Bosse, and A. Bayer: “Laser applications in microtechnology,” J. Mater. Process. Technol., 167, (2005) 494.

[8] IPG Photonics: High-efficiency lasers, https://www.ipgphotonics.com/de/technology/high-efficiency-lasers (accessed 30 June 2025).

[9] S. Zhao, Z. Tan, H. Wang, and M. Gao: “Effects of spreading behaviors on dynamic reflectivity in laser soldering,” Opt. Laser Technol., 155, (2022) 108404.

[10] M. Kanskar, T. Earles, T. Goodnough, E. Stiers, D. Botez, and L. Mawst: “73% CW power conversion efficiency at 50 W from 970 nm diode laser bars,” Electron. Lett., 41, (2005) 245.

[11] H. Tatsumi, S. Kaneshita, Y. Kida, Y. Sato, M. Tsukamoto, and H. Nishikawa: “Highly efficient soldering of Sn-Ag-Cu solder joints using blue laser,” J. Manuf. Process., 82, (2022) 700.

[12] A. Häusler: Präzisionserhöhung beim Laserstrahl-Mikroschweißen durch angepasstes Energiemanagement, (Apprimus Verlag, Aachen, 2021) p.60.

[13] E. D. Palik: Handbook of Optical Constants of Solids, (Academic Press, 1998) p.280.

[14] W. M. Steen and J. Mazumder: Laser Material Processing, 4th ed. (Springer, London, 2010) p.205.

[15] M.-S. Jeong, M.-H. Heo, J. Kim, and J.-W. Yoon: "A comparative study of laser soldering and reflow soldering using Sn–58Bi solder/Cu joints," J. Mater. Sci.: Mater. Electron., 34, (2023) 1960.

(Received: June 30, 2025, Accepted: April 5, 2026)